Monthly Notices
of the
ROYAL ASTRONOMICAL SOCIETY

MNRAS **447,** 711–721 (2015) doi:10.1093/mnras/stu2394

High-precision photometry by telescope defocusing – VII. The ultrashort period planet WASP-103⋆

John Southworth,[1]† L. Mancini,[2] S. Ciceri,[2] J. Budaj,[3,4] M. Dominik,[5]‡ R. Figuera Jaimes,[5,6] T. Haugbølle,[7] U. G. Jørgensen,[8] A. Popovas,[8] M. Rabus,[2,9] S. Rahvar,[10] C. von Essen,[11] R. W. Schmidt,[12] O. Wertz,[13] K. A. Alsubai,[14] V. Bozza,[15,16] D. M. Bramich,[14] S. Calchi Novati,[17,15,18]§ G. D'Ago,[15,16] T. C. Hinse,[19] Th. Henning,[2] M. Hundertmark,[5] D. Juncher,[8] H. Korhonen,[8,20] J. Skottfelt,[8] C. Snodgrass,[21] D. Starkey[5] and J. Surdej[13]

Affiliations are listed at the end of the paper

Accepted 2014 November 11. Received 2014 October 20; in original form 2014 September 2

ABSTRACT

We present 17 transit light curves of the ultrashort period planetary system WASP-103, a strong candidate for the detection of tidally-induced orbital decay. We use these to establish a high-precision reference epoch for transit timing studies. The time of the reference transit mid-point is now measured to an accuracy of 4.8 s, versus 67.4 s in the discovery paper, aiding future searches for orbital decay. With the help of published spectroscopic measurements and theoretical stellar models, we determine the physical properties of the system to high precision and present a detailed error budget for these calculations. The planet has a Roche lobe filling factor of 0.58, leading to a significant asphericity; we correct its measured mass and mean density for this phenomenon. A high-resolution *Lucky Imaging* observation shows no evidence for faint stars close enough to contaminate the point spread function of WASP-103. Our data were obtained in the Bessell *RI* and the SDSS *griz* passbands and yield a larger planet radius at bluer optical wavelengths, to a confidence level of 7.3σ. Interpreting this as an effect of Rayleigh scattering in the planetary atmosphere leads to a measurement of the planetary mass which is too small by a factor of 5, implying that Rayleigh scattering is not the main cause of the variation of radius with wavelength.

Key words: stars: fundamental parameters – stars: individual: WASP-103 – planetary systems.

1 INTRODUCTION

An important factor governing the tidal evolution of planetary systems is the stellar tidal quality factor $Q_\star$ (e.g. Goldreich & Soter 1966), which represents the efficiency of tidal dissipation in the star. Its value is necessary for predicting the time-scales of orbital circularization, axial alignment and rotational synchronization of binary star and planet systems. Short-period giant planets suffer orbital decay due to tidal effects, and most will ultimately be devoured by their host star rather than reach an equilibrium state (Jackson, Barnes & Greenberg 2009; Levrard, Winisdoerffer & Chabrier 2009). The magnitude of $Q_\star$ therefore influences the orbital period distribution of populations of extrasolar planets.

Unfortunately, $Q_\star$ is not well constrained by current observations. Its value is often taken to be 10^6 (Ogilvie & Lin 2007) but there exist divergent results in the literature. A value of $10^{5.5}$ was found to be a good match to a sample of known extrasolar planets by Jackson, Greenberg & Barnes (2008), but theoretical work by Penev & Sasselov (2011) constrained $Q_\star$ to lie between 10^8 and $10^{9.5}$ and an observational study by Penev et al. (2012) found $Q_\star > 10^7$ to 99 per cent confidence. Inferences from the properties of binary star systems are often used but are not relevant to this issue: $Q_\star$ is not a fundamental property of a star but depends on the nature of the tidal perturbation (Goldreich 1963; Ogilvie 2014). $Q_\star$ should however be

⋆ Based on data collected by MiNDSTEp with the Danish 1.54 m telescope, and data collected with GROND on the MPG 2.2 m telescope, both located at ESO La Silla.

† E-mail: astro.js@keele.ac.uk
‡ Royal Society University Research Fellow.
§ Sagan visiting fellow.

Table 1. Log of the observations presented in this work. N_{obs} is the number of observations, T_{exp} is the exposure time, T_{dead} is the dead time between exposures, 'Moon illum'. is the fractional illumination of the Moon at the mid-point of the transit, and N_{poly} is the order of the polynomial fitted to the out-of-transit data. The aperture radii are target aperture, inner sky and outer sky, respectively.

Instrument	Date of first obs	Start time (UT)	End time (UT)	N_{obs}	T_{exp} (s)	T_{dead} (s)	Filter	Airmass	Moon illum.	Aperture radii (pixel)	N_{poly}	Scatter (mmag)
DFOSC	2014 04 20	05:08	09:45	134	100–105	18	*R*	1.54 → 1.24 → 1.54	0.725	14 25 45	1	0.675
DFOSC	2014 05 02	05:45	10:13	113	110–130	19	*I*	1.28 → 1.24 → 2.23	0.100	14 22 50	1	0.815
DFOSC	2014 06 09	04:08	08:22	130	100	16	*R*	1.24 → 3.08	0.888	16 27 50	1	1.031
DFOSC	2014 06 23	01:44	06:19	195	50–120	16	*R*	1.35 → 1.24 → 1.86	0.168	14 22 40	1	1.329
DFOSC	2014 06 24	00:50	04:25	112	100	16	*R*	1.54 → 1.24 → 1.31	0.103	19 25 40	1	0.647
DFOSC	2014 07 06	01:28	05:20	118	100	18	*R*	1.28 → 1.24 → 1.80	0.564	16 26 50	1	0.653
DFOSC	2014 07 18	01:19	05:45	139	90–110	16	*R*	1.25 → 3.00	0.603	17 25 60	1	0.716
DFOSC	2014 07 18	23:04	04:20	181	60–110	16	*R*	1.52 → 1.24 → 1.73	0.502	16 24 55	2	0.585
GROND	2014 07 06	00:23	05:27	122	100–120	40	*g*	1.45 → 1.24 → 1.87	0.564	24 65 85	2	1.251
GROND	2014 07 06	00:23	05:27	119	100–120	40	*r*	1.45 → 1.24 → 1.87	0.564	24 65 85	2	0.707
GROND	2014 07 06	00:23	05:27	125	100–120	40	*i*	1.45 → 1.24 → 1.87	0.564	24 65 85	2	0.843
GROND	2014 07 06	00:23	05:27	121	100–120	40	*z*	1.45 → 1.24 → 1.87	0.564	24 65 85	2	1.106
GROND	2014 07 18	22:55	03:59	125	98–108	41	*g*	1.64 → 1.24 → 1.93	0.502	30 50 85	2	0.882
GROND	2014 07 18	22:55	04:43	143	98–108	41	*r*	1.64 → 1.24 → 1.93	0.502	25 45 70	2	0.915
GROND	2014 07 18	22:55	04:39	142	98–108	41	*i*	1.64 → 1.24 → 1.88	0.502	28 56 83	2	0.656
GROND	2014 07 18	22:55	04:43	144	98–108	41	*z*	1.64 → 1.24 → 1.93	0.502	30 50 80	2	0.948
CASLEO	2014 08 12	23:22	03:10	129	90–120	4	*R*	1.29 → 2.12	0.920	20 30 60	4	1.552

observationally accessible through the study of transiting extrasolar planets (TEPs).

Birkby et al. (2014) assessed the known population of TEPs for their potential for the direct determination of the strength of tidal interactions. The mechanism considered was the detection of tidally-induced orbital decay, which manifests itself as a decreasing orbital period. These authors found that WASP-18 (Hellier et al. 2009; Southworth et al. 2009b) is the most promising system, due to its short orbital period (0.94 d) and large planet mass (10.4 M_{Jup}), followed by WASP-103 (Gillon et al. 2014, hereafter G14), then WASP-19 (Hebb et al. 2010; Mancini et al. 2013).

Adopting the canonical value of $Q_\star = 10^6$, Birkby et al. (2014) calculated that orbital decay would cause a shift in transit times – over a time interval of 10 yr – of 350 s for WASP-18, 100 s for WASP-103 and 60 s for WASP-19. Detection of this effect clearly requires observations over many years coupled with a precise ephemeris against which to measure deviations from strict periodicity. High-quality transit timing data are already available for WASP-18 (Maxted et al. 2013) and WASP-19 (Abe et al. 2013; Lendl et al. 2013; Mancini et al. 2013; Tregloan-Reed, Southworth & Tappert 2013), but not for WASP-103.

WASP-103 was discovered by G14 and comprises a TEP of mass 1.5 M_{Jup} and radius 1.6 R_{Jup} in a very short-period orbit (0.92 d) around an F8 V star of mass 1.2 $M_\odot$ and radius 1.4 $R_\odot$. G14 obtained observations of five transits, two with the Swiss Euler telescope and three with TRAPPIST, both at ESO La Silla. The Euler data each cover only half a transit, whereas the TRAPPIST data have a lower photometric precision and suffer from 180° field rotations during the transits due to the nature of the telescope mount. The properties of the system could therefore be measured to only modest precision; in particular the ephemeris zero-point is known to a precision of only 64 s. In this work, we present 17 high-quality transit light curves which we use to determine a precise orbital ephemeris for WASP-103, as well as to improve measurements of its physical properties.

2 OBSERVATIONS AND DATA REDUCTION

2.1 DFOSC observations

Eight transits were obtained using the DFOSC (Danish Faint Object Spectrograph and Camera) instrument on the 1.54 m Danish Telescope at ESO La Silla, Chile, in the context of the MiNDSTEp microlensing programme (Dominik et al. 2010). DFOSC has a field of view of 13.7 arcmin×13.7 arcmin at a plate scale of 0.39 arcsec pixel^{-1}. We windowed down the CCD to cover WASP-103 itself and seven good comparison stars, in order to shorten the dead time between exposures.

The instrument was defocused to lower the noise level of the observations, in line with our usual strategy (see Southworth et al. 2009a, 2014). The telescope was autoguided to limit pointing drifts to less than five pixels over each observing sequence. Seven of the transits were obtained through a Bessell *R* filter, but one was taken through a Bessell *I* filter by accident. An observing log is given in Table 1 and the light curves are plotted individually in Fig. 1.

2.2 GROND observations

We observed two transits of WASP-103 using the GROND instrument (Greiner et al. 2008) mounted on the MPG 2.2 m telescope at La Silla, Chile. Both transits were also observed with DFOSC. GROND was used to obtain light curves simultaneously in passbands which approximate SDSS *g*, *r*, *i* and *z*. The small field of view of this instrument (5.4 arcmin×5.4 arcmin at a plate scale of 0.158 arcsec pixel^{-1}) meant that few comparison stars were available and the best of these was several times fainter than WASP-103 itself. The scatter in the GROND light curves is therefore worse than generally achieved (e.g. Nikolov et al. 2013; Mancini et al. 2014b,c), but the data are certainly still useful. The telescope was defocused and autoguided for both sets of observations. Further details are given in the observing log (Table 1) and the light curves are plotted individually in Fig. 2.

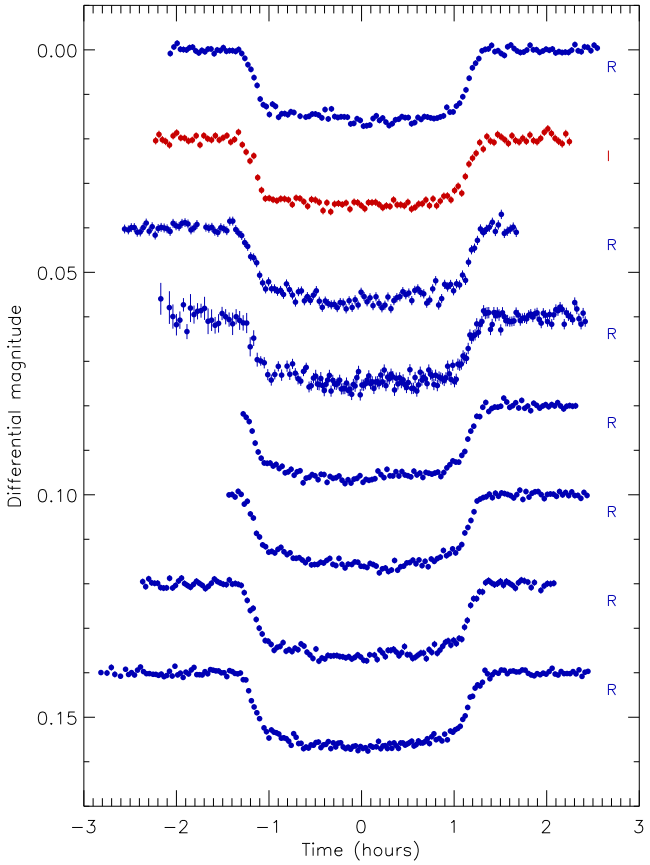

Figure 1. DFOSC light curves presented in this work, in the order they are given in Table 1. Times are given relative to the mid-point of each transit, and the filter used is indicated. Dark blue and dark red filled circles represent observations through the Bessell *R* and *I* filters, respectively.

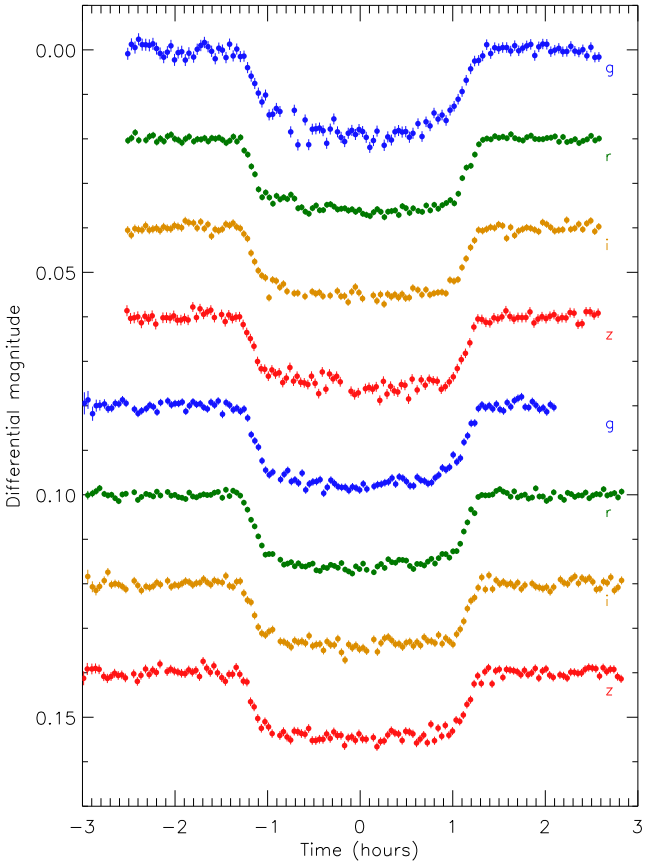

Figure 2. GROND light curves presented in this work, in the order they are given in Table 1. Times are given relative to the mid-point of each transit, and the filter used is indicated. *g*-band data are shown in light blue, *r*-band in green, *i*-band in orange and *z*-band in light red.

2.3 CASLEO observations

We observed one transit of WASP-103 (Fig. 3) using the 2.15 m Jorge Sahade telescope located at the Complejo Astronómico El Leoncito (CASLEO) in San Juan, Argentina.[1] We used the focal reducer and Roper Scientific CCD, yielding an unvignetted field of view of 9 arcmin radius at a plate scale of 0.45 arcsec pixel^{-1}. The CCD was operated without binning or windowing due to its short readout time. The observing conditions were excellent. The images were slightly defocused to a full width at half-maximum (FWHM) of 3 arcsec, and were obtained through a Johnson–Cousins Schuler *R* filter.

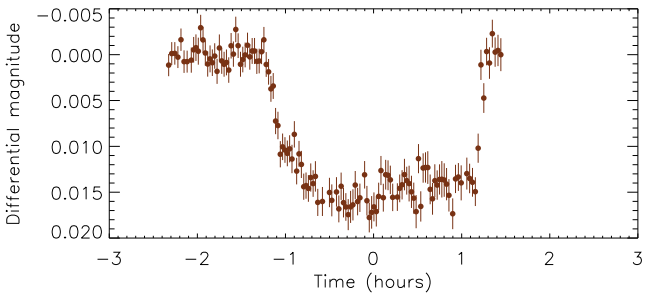

Figure 3. The CASLEO light curve of WASP-103. Times are given relative to the mid-point of the transit.

2.4 Data reduction

The DFOSC and GROND data were reduced using the DEFOT code (Southworth et al. 2009a) with the improvements discussed by Southworth et al. (2014). Master bias, dome flat-fields and sky flat-fields were constructed but not applied, as they were found not to improve the quality of the resulting light curves (see Southworth et al. 2014). Aperture photometry was performed using the IDL[2]/ASTROLIB[3] implementation of DAOPHOT (Stetson 1987). Image motion was tracked by cross-correlating individual images with a reference image.

We obtained photometry on the instrumental system using software apertures of a range of sizes, and retained those which gave light curves with the smallest scatter (Table 1). We found that the

[1] Visiting Astronomer, Complejo Astronómico El Leoncito operated under agreement between the Consejo Nacional de Investigaciones Científicas y Técnicas de la República Argentina and the National Universities of La Plata, Córdoba and San Juan.

[2] The acronym IDL stands for Interactive Data Language and is a trademark of ITT Visual Information Solutions. For further details see: http://www.exelisvis.com/ProductsServices/IDL.aspx.

[3] The ASTROLIB subroutine library is distributed by NASA. For further details see: http://idlastro.gsfc.nasa.gov/.

Table 2. Sample of the data presented in this work (the first data point of each light curve). The full data set will be made available at the CDS.

Instrument	Filter	BJD(TDB)	Diff. mag.	Uncertainty
DFOSC	*R*	2456767.719670	0.000 8211	0.000 6953
DFOSC	*I*	2456779.746022	0.000 4141	0.000 8471
DFOSC	*R*	2456817.679055	0.000 2629	0.000 9941
DFOSC	*R*	2456831.578063	− 0.004 0473	0.003 5872
DFOSC	*R*	2456832.540736	0.001 8135	0.000 6501
DFOSC	*R*	2456844.566748	0.000 0224	0.000 6405
DFOSC	*R*	2456856.559865	− 0.000 4751	0.000 6952
DFOSC	*R*	2456857.466519	− 0.000 0459	0.000 5428
GROND	*g*	2456844.521804	0.000 8698	0.001 3610
GROND	*r*	2456844.521804	0.000 3845	0.000 7863
GROND	*i*	2456844.521804	0.000 5408	0.000 9272
GROND	*z*	2456844.521804	− 0.001 3755	0.001 2409
GROND	*g*	2456857.459724	− 0.000 5583	0.002 4887
GROND	*r*	2456857.461385	0.000 0852	0.000 9575
GROND	*i*	2456857.461385	− 0.001 6371	0.001 5169
GROND	*z*	2456857.459724	0.001 2460	0.001 5680
CASLEO	*R*	2456882.47535	0.001 14	0.001 21

choice of aperture size does influence the scatter in the final light curve, but does not have a significant effect on the transit shape.

The instrumental magnitudes were then transformed to differential-magnitude light curves normalized to zero magnitude outside transit. The normalization was enforced with first- or second-order polynomials (see Table 1) fitted to the out-of-transit data. The differential magnitudes are relative to a weighted ensemble of typically five (DFOSC) or two to four (GROND) comparison stars. The comparison star weights and polynomial coefficients were simultaneously optimized to minimize the scatter in the out-of-transit data.

The CASLEO data were reduced using standard aperture photometry methods, with the IRAF tasks CCDPROC and APPHOT. We found that it was necessary to flat-field the data in order to obtain a good light curve. The final light curve was obtained by dividing the flux of WASP-103 by the average flux of three comparison stars. An aperture radius of three times the FWHM was used, as it minimized the scatter in the data.

Finally, the timestamps for the data points were converted to the BJD(TDB) time-scale (Eastman, Siverd & Gaudi 2010). We performed manual time checks for several images and have verified that the FITS file timestamps are on the UTC system to within a few seconds. The reduced data are given in Table 2 and will be lodged with the CDS.[4]

2.5 High-resolution imaging

Several images were taken of WASP-103 with DFOSC in sharp focus, in order to test for the presence of faint nearby stars whose photons might bias our results (Daemgen et al. 2009). The closest star we found on any image is 42 pixels south-east of WASP-103, and 5.3 mag fainter in the *R* band. It is thus too faint and far away to contaminate the inner aperture of our target star.

We proceeded to obtain a high-resolution image of WASP-103 using the Lucky Imager (LI) mounted on the Danish telescope (see Skottfelt et al. 2013). The LI uses an Andor 512×512 pixel electron-multiplying CCD, with a pixel scale of 0.09 arcsec pixel^{-1} giving a field of view of 45 arcsec × 45 arcsec. The data were reduced using a dedicated pipeline and the 2 per cent of images with the smallest point spread function (PSF) were stacked together to yield combined images whose PSF is smaller than the seeing limit. A long-pass filter was used, resulting in a response which approximates that of SDSS i+z. An overall exposure time of 415 s corresponds to an effective exposure time of 8.3 s for the best 2 per cent of the images. The FWHM of the PSF is 5.9 pixels (0.53 arcsec) in both dimensions. The LI image (Fig. 4) shows no evidence for a point source closer than that found in our DFOSC images.

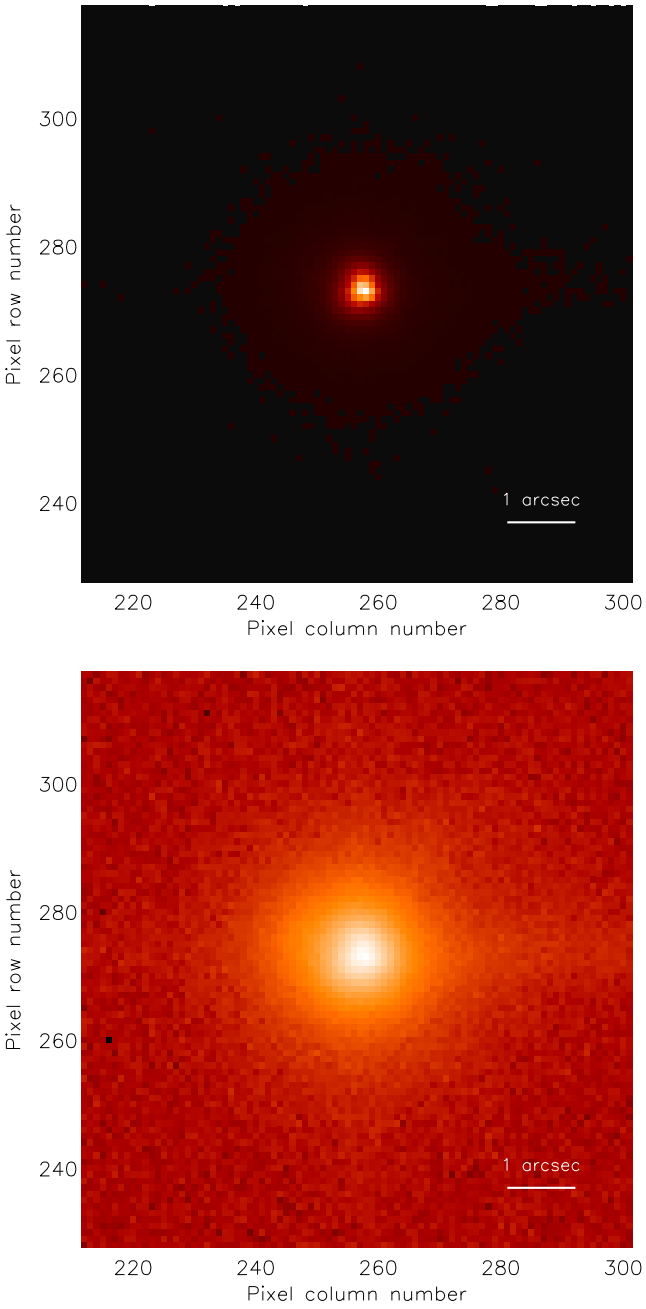

Figure 4. High-resolution Lucky Image of the field around WASP-103. The upper panel has a linear flux scale for context and the lower panel has a logarithmic flux scale to enhance the visibility of any faint stars. Each image covers 8 arcsec × 8 arcsec centred on WASP-103. A bar of length 1 arcsec is superimposed in the bottom right of each image. The image is a sum of the best 2 per cent of the original images.

[4] http://vizier.u-strasbg.fr/

Table 3. Times of minimum light and their residuals versus the ephemeris derived in this work.

Time of min. (BJD/TDB)	Error (d)	Cycle number	Residual (d)	Reference
2456459.59957	0.000 79	−407.0	0.000 19	G14
2456767.80578	0.000 17	−74.0	−0.000 29	This work (DFOSC *R*)
2456779.83870	0.000 22	−61.0	0.000 54	This work (DFOSC *I*)
2456817.78572	0.000 27	−20.0	0.000 19	This work (DFOSC *R*)
2456831.66843	0.000 39	−5.0	−0.000 29	This work (DFOSC *R*)
2456832.59401	0.000 24	−4.0	−0.000 25	This work (DFOSC *R*)
2456844.62641	0.000 19	9.0	0.000 05	This work (DFOSC *R*)
2456844.62642	0.000 34	9.0	0.000 06	This work (GROND *g*)
2456844.62633	0.000 19	9.0	−0.000 03	This work (GROND *r*)
2456844.62647	0.000 23	9.0	0.000 11	This work (GROND *i*)
2456844.62678	0.000 30	9.0	0.000 42	This work (GROND *z*)
2456856.65838	0.000 18	22.0	−0.000 07	This work (DFOSC *R*)
2456857.58383	0.000 14	23.0	−0.000 16	This work (DFOSC *R*)
2456857.58390	0.000 22	23.0	−0.000 09	This work (GROND *g*)
2456857.58398	0.000 17	23.0	0.000 01	This work (GROND *r*)
2456857.58400	0.000 25	23.0	0.000 01	This work (GROND *i*)
2456857.58421	0.000 25	23.0	0.000 22	This work (GROND *z*)
2456882.57473	0.000 50	50.0	0.001 00	This work (CASLEO *R*)

3 TRANSIT TIMING ANALYSIS

We first modelled each light curve individually using the JKTEBOP code (see below) in order to determine the times of mid-transit. In this process, the error bars for each data set were also scaled to give a reduced χ^2 of $\chi^2_\nu = 1.0$ versus the fitted model. This step is needed because the uncertainties from the APER algorithm are often moderately underestimated.

We then fitted the times of mid-transit with a straight line versus cycle number to determine a new linear orbital ephemeris. We included the ephemeris zero-point from G14, which is also on the BJD(TDB) time-scale and was obtained by them from a joint fit to all their data. Table 3 gives all transit times plus their residual versus the fitted ephemeris. We chose the reference epoch to be that which gives the lowest uncertainty in the time zero-point, as this minimizes the covariance between the reference time of minimum and the orbital period. The resulting ephemeris is

$$T_0 = \mathrm{BJD(TDB)}\ 2456836.296445(55) + 0.9255456(13) \times E,$$

where E gives the cycle count versus the reference epoch and the bracketed quantities indicate the uncertainty in the final digit of the preceding number.

The χ^2_ν of the fit is excellent at 1.055. The timestamps from DFOSC and GROND are obtained from different atomic clocks, so are unrelated to each other. The good agreement between them is therefore evidence that both are correct.

Fig. 5 shows the residuals of the times of mid-transit versus the linear ephemeris we have determined. The precision in the measurement of the mid-point of the reference transit has improved from 64.7 s (G14) to 4.8 s, meaning that we have established a high-quality set of timing data against which orbital decay could be measured in future.

4 LIGHT-CURVE ANALYSIS

We analysed our light curves using the JKTEBOP[5] code (Southworth, Maxted & Smalley 2004) and the *Homogeneous Studies* methodology (Southworth 2012, and references therein). The light curves were divided up according to their passband (Bessell *R* and *I* for DFOSC and SDSS *griz* for GROND) and each set was modelled together.

The model was parametrized by the fractional radii of the star and the planet (r_A and r_b), which are the ratios between the true radii and the semimajor axis ($r_\mathrm{A,b} = \frac{R_\mathrm{A,b}}{a}$). The parameters of the fit were the sum and ratio of the fractional radii ($r_\mathrm{A} + r_\mathrm{b}$ and $k = \frac{r_\mathrm{b}}{r_\mathrm{A}}$), the orbital inclination (i), limb darkening coefficients, and a reference time of mid-transit. We assumed an orbital eccentricity of zero (G14) and the orbital period found in Section 3. We also fitted for the coefficients of polynomial functions of differential magnitude versus time (Southworth et al. 2014). One polynomial was used for each transit light curve, of the order given in Table 1.

Limb darkening was incorporated using each of five laws (see Southworth 2008), with the linear coefficients either fixed at theoretically predicted values[6] or included as fitted parameters. We did not calculate fits for both limb darkening coefficients in the four two-coefficient laws as they are very strongly correlated (Southworth, Bruntt & Buzasi 2007b; Carter et al. 2008). The non-linear coefficients were instead perturbed by ±0.1 on a flat distribution during the error analysis simulations, in order to account for imperfections in the theoretical values of the coefficients.

Error estimates for the fitted parameters were obtained in three ways. Two sets were obtained using residual-permutation and Monte Carlo simulations (Southworth 2008) and the larger of the two was retained for each fitted parameter. We also ran solutions using the five different limb darkening laws, and increased the error bar for each parameter to account for any disagreement between these five solutions. Tables of results for each light curve can be found in the appendix and the best fits can be inspected in Fig. 6.

4.1 Results

For all light curves, we found that the best solutions were obtained when the linear limb darkening coefficient was fitted and the non-linear coefficient was fixed but perturbed. We found that there is a significant correlation between i and k for all light curves, which hinders the precision to which we can measure the photometric parameters. The best fit for the CASLEO and the GROND *z*-band data is a central transit ($i \approx 90^\circ$), but this does not have a significant effect on the value of k measured from these data.

Table 4 holds the measured parameters from each light curve. The final value for each parameter is the weighted mean of the values from the different light curves. We find good agreement for all parameters except for k, which is in line with previous experience (see Southworth 2012 and references therein). The χ^2_ν of the individual values of k versus the weighted mean is 3.1, and the error bar for the final value of k in Table 4 has been multiplied by $\sqrt{3.1}$ to force a χ^2_ν of unity. Our results agree with, but are significantly more precise than, those found by G14.

5 PHYSICAL PROPERTIES

We have measured the physical properties of the WASP-103 system using the results from Section 4, five grids of predictions from theoretical models of stellar evolution (Claret 2004; Demarque et al.

[5] JKTEBOP is written in FORTRAN77 and the source code is available at http://www.astro.keele.ac.uk/jkt/codes/jktebop.html.

[6] Theoretical limb darkening coefficients were obtained by bilinear interpolation in T_eff and $\log g$ using the JKTLD code available from: http://www.astro.keele.ac.uk/jkt/codes/jktld.html.

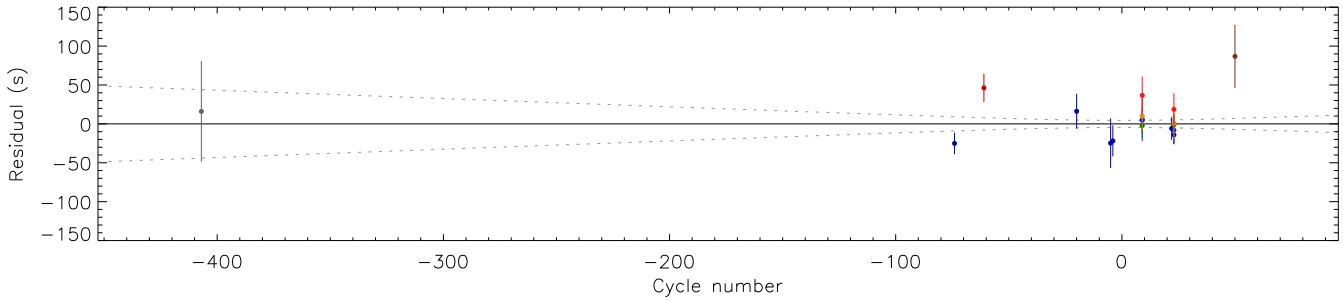

Figure 5. Plot of the residuals of the timings of mid-transit for WASP-103 versus a linear ephemeris. The leftmost point is from G14 and the remaining points are from the current work (colour-coded consistently with Figs 1–3). The dotted lines show the 1σ uncertainty in the ephemeris as a function of cycle number.

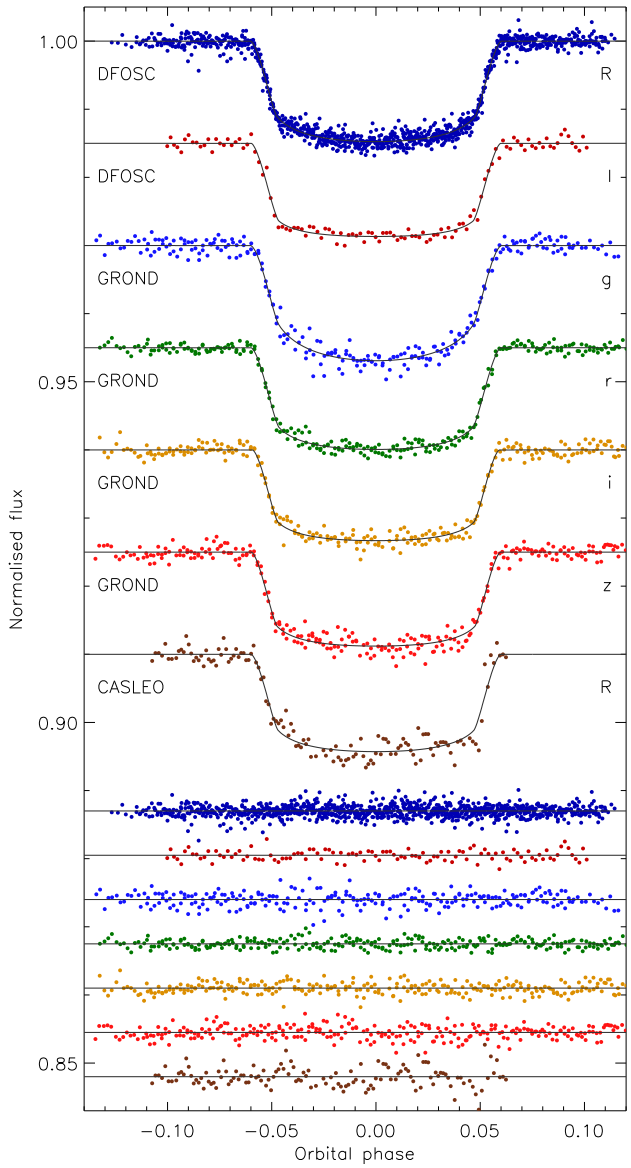

Figure 6. Phased light curves of WASP-103 compared to the JKTEBOP best fits. The residuals of the fits are plotted at the base of the figure, offset from unity. Labels give the source and passband for each data set. The polynomial baseline functions have been removed from the data before plotting.

2004; Pietrinferni et al. 2004; VandenBerg, Bergbusch & Dowler 2006; Dotter et al. 2008), and the spectroscopic properties of the host star. Theoretical models are needed to provide an additional constraint on the stellar properties as the system properties cannot be obtained from only measured quantities. The spectroscopic properties were obtained by G14 and comprise effective temperature ($T_{\rm eff} = 6110 \pm 160$ K), metallicity ([Fe/H] $= 0.06 \pm 0.13$) and velocity amplitude ($K_{\rm A} = 271 \pm 15$ m s^{-1}). The adopted set of physical constants is given in Southworth (2011).

We first estimated the velocity amplitude of the *planet*, $K_{\rm b}$, and used this along with the measured $r_{\rm A}$, $r_{\rm b}$, i and $K_{\rm A}$ to determine the physical properties of the system. $K_{\rm b}$ was then iteratively refined to find the best match between the measured $r_{\rm A}$ and the calculated $\frac{R_{\rm A}}{a}$, and the observed $T_{\rm eff}$ and that predicted by a theoretical model for the obtained stellar mass, radius and [Fe/H]. This was done for a grid of ages from the zero-age main sequence to beyond the terminal-age main sequence for the star, in 0.01 Gyr increments, and the overall best $K_{\rm b}$ was adopted. The statistical errors in the input quantities were propagated to the output quantities by a perturbation approach.

We ran the above analysis for each of the five grids of theoretical stellar models, yielding five different estimates of each output quantity. These were transformed into a single final result for each parameter by taking the unweighted mean of the five estimates and their statistical errors, plus an accompanying systematic error which gives the largest difference between the mean and individual values. The final results of this process are a set of physical properties for the WASP-103 system, each with a statistical error and a systematic error. The stellar density, planetary surface gravity and planetary equilibrium temperatures can be calculated without resorting to theoretical predictions (Seager & Mallén-Ornelas 2003; Southworth, Wheatley & Sams 2007a; Southworth 2010), so do not have an associated systematic error.

5.1 Results

Our final results are given in Table 5 and have been added to TEPCat.[7] We find good agreement between the five different model sets (table A8). Some of the measured quantities, in particular the stellar and planetary mass, are still relatively uncertain. To investigate this we calculated a complete error budget for each output parameter, and show the results of this analysis in Table 6 when using the Y^2 theoretical stellar models (Demarque et al. 2004). The error budgets for the other four model sets are similar.

[7] TEPCat is The Transiting Extrasolar Planet Catalogue (Southworth 2011) at: http://www.astro.keele.ac.uk/jkt/tepcat/.

Table 4. Parameters of the fit to the light curves of WASP-103 from the JKTEBOP analysis (top). The final parameters are given in bold and the parameters found by G14 are given below this. Quantities without quoted uncertainties were not given by G14 but have been calculated from other parameters which were. The error bar for the final value of k has been inflated to account for the disagreement between different measurements.

Source	$r_A + r_b$	k	i (°)	r_A	r_b
DFOSC *R* band	0.3703 ± 0.0055	0.1129 ± 0.0009	88.1 ± 2.2	0.3328 ± 0.0048	0.037 55 ± 0.000 74
DFOSC *I* band	0.3766 ± 0.0146	0.1118 ± 0.0013	84.8 ± 4.2	0.3387 ± 0.0128	0.037 88 ± 0.001 75
GROND *g* band	0.3734 ± 0.0140	0.1183 ± 0.0022	86.3 ± 3.9	0.3339 ± 0.0123	0.039 49 ± 0.002 01
GROND *r* band	0.3753 ± 0.0102	0.1150 ± 0.0011	85.2 ± 3.2	0.3366 ± 0.0087	0.038 70 ± 0.001 24
GROND *i* band	0.3667 ± 0.0132	0.1091 ± 0.0017	87.1 ± 3.6	0.3307 ± 0.0116	0.036 06 ± 0.001 29
GROND *z* band	0.3661 ± 0.0111	0.1106 ± 0.0016	89.9 ± 2.4	0.3297 ± 0.0099	0.036 45 ± 0.001 20
CASLEO *R* band	0.3665 ± 0.0203	0.1117 ± 0.0055	89.6 ± 4.5	0.3296 ± 0.0167	0.036 83 ± 0.003 16
Final results	**0.3712 ± 0.0040**	**0.1127 ± 0.0009**	**87.3 ± 1.2**	**0.3335 ± 0.0035**	**0.037 54 ± 0.000 49**
G14	0.3725	$0.1093^{+0.0019}_{-0.0017}$	86.3 ± 2.7	$0.3358^{+0.0111}_{-0.0055}$	0.03670

Table 5. Derived physical properties of WASP-103. Quantities marked with a ⋆ are significantly affected by the spherical approximation used to model the light curves, and revised values are given at the base of the table.

Quantity	Symbol	Unit	This work	G14
Stellar mass	M_A	$M_\odot$	1.204 ± 0.089 ± 0.019	$1.220^{+0.039}_{-0.036}$
Stellar radius	R_A	$R_\odot$	1.419 ± 0.039 ± 0.008	$1.436^{+0.052}_{-0.031}$
Stellar surface gravity	$\log g_A$	cgs	4.215 ± 0.014 ± 0.002	$4.22^{+0.12}_{-0.05}$
Stellar density	ρ_A	$\rho_\odot$	0.421 ± 0.013	$0.414^{+0.021}_{-0.039}$
Planet mass	M_b	M_{Jup}	1.47 ± 0.11 ± 0.02	1.490 ± 0.088
Planet radius⋆	R_b	R_{Jup}	1.554 ± 0.044 ± 0.008	$1.528^{+0.073}_{-0.047}$
Planet surface gravity	g_b	$m\,s^{-2}$	15.12 ± 0.93	15.7 ± 1.4
Planet density⋆	ρ_b	ρ_{Jup}	0.367 ± 0.027 ± 0.002	$0.415^{+0.046}_{-0.053}$
Equilibrium temperature	T'_{eq}	K	2495 ± 66	2508^{+75}_{-70}
Safronov number	Θ		0.0311 ± 0.0019 ± 0.0002	
Orbital semimajor axis	a	au	0.019 78 ± 0.000 49 ± 0.000 10	0.019 85 ± 0.000 21
Age	τ	Gyr	$3.8\,^{+2.1}_{-1.6}\,^{+0.3}_{-0.4}$	3 to 5
Planetary parameters corrected for asphericity:				
Planet radius		R_{Jup}	1.603 ± 0.052	
Planet density		ρ_{Jup}	0.335 ± 0.025	

Table 6. Detailed error budget for the calculation of the system properties of WASP-103 from the photometric and spectroscopic parameters, and the Y^2 stellar models. Each number in the table is the fractional contribution to the final uncertainty of an output parameter from the error bar of an input parameter. The final uncertainty for each output parameter is the quadrature sum of the individual contributions from each input parameter.

Output parameter	Input parameter K_A	i	r_A	r_b	T_{eff}	[Fe/H]
Age	0.012		0.035		0.873	0.471
a	0.030		0.020		0.797	0.601
M_A	0.029		0.020		0.796	0.602
R_A	0.027		0.469		0.703	0.530
$\log g_A$	0.019		0.706		0.563	0.424
ρ_A	0.002		1.000		0.001	
M_b	0.809	0.014	0.012		0.466	0.352
R_b	0.025		0.017	0.544	0.668	0.504
g_b	0.901	0.016		0.434		
ρ_b	0.772	0.014	0.006	0.564	0.232	0.174

The uncertainties in the physical properties of the planet are dominated by that in K_A, followed by that in r_b. The uncertainties in the stellar properties are dominated by those in T_{eff} and [Fe/H], followed by r_A. Improvements in our understanding of the WASP-103 system would most easily be achieved by obtaining new spectra from which additional radial velocity measurements and improved T_{eff} and [Fe/H] measurements could be obtained.

To illustrate the progress possible from further spectroscopic analysis, we reran the analysis but with smaller errorbars of ±50 K in T_{eff} and ±0.05 dex in [Fe/H]. The precision in M_A changes from 0.091 to 0.041 $M_\odot$. Similar improvements are seen for a, and smaller improvements for R_A, R_b and ρ_b. Augmenting this situation by adopting an error bar of $\pm 5\,m\,s^{-1}$ in K_A changes the precision in M_b from 0.11 to 0.047 M_{Jup} and yields further improvements for R_b and ρ_b.

5.2 Comparison with G14

Table 5 also shows the parameter values found by G14, which are in good agreement with our results. Some of the error bars however

are smaller than those in the current work, despite the fact that G14 had much less observational data at their disposal. A possible reason for this discrepancy is the additional constraint used to obtain a determinate model for the system. We used each of five sets of theoretical model predictions, whilst G14 adopted a calibration of $M_{\rm A}$ as a function of $\rho_{\rm A}$, $T_{\rm eff}$ and [Fe/H] based on semi-empirical results from the analysis of low-mass detached eclipsing binary (dEB) systems (Torres, Winn & Holman 2008; Southworth 2009, 2011; Enoch et al. 2010). The dEB calibration suffers from an astrophysical scatter of the calibrating objects which is much greater than that of the precision to which the calibration function can be fitted (see Southworth 2011). G14 accounted for the uncertainty in the calibration by perturbing the measured properties of the calibrators during their Markov chain Monte Carlo analysis (Gillon et al. 2013). They therefore accounted for the observational uncertainties in the measured properties of the calibrators, but neglected the astrophysical scatter.

There is supporting evidence for this interpretation of why our error bars for some measurements are significantly larger than those found by G14. Our own implementation of the dEB calibration (Southworth 2011) explicitly includes the astrophysical scatter and yields $M_{\rm A} = 1.29 \pm 0.11\,{\rm M}_{\odot}$, where the greatest contribution to the uncertainty is the scatter of the calibrators around the calibration function. G14 themselves found a value of $M_{\rm A} = 1.18 \pm 0.10\,{\rm M}_{\odot}$ from an alternative approach (comparable to our main method) of using the CLÉS theoretical models (Scuflaire et al. 2008) as their additional constraint. This is much less precise than their default value of $M_{\rm A} = 1.220^{+0.039}_{-0.036}\,{\rm M}_{\odot}$ from the dEB calibration. Gillon (private communication) confirms our interpretation of the situation.

5.3 Correction for asphericity

As pointed out by Li et al. (2010) for the case of WASP-12 b, some close-in extrasolar planets may have significant departures from spherical shape. Budaj (2011) calculated the Roche shapes of all transiting planets known at that time, as well as light curves and spectra taking into account the non-spherical shape. He found that WASP-19 b and WASP-12 b had the most significant tidal distortion of all known planets. The Roche model assumes that the object is rotating synchronously with the orbital period, there is a negligible orbital eccentricity, and that masses can be treated as point masses. The Roche shape has a characteristic pronounced expansion of the object towards the substellar point, and a slightly less pronounced expansion towards the antistellar point. The radii on the side of the object are smaller, and the radii at the rotation poles are the smallest. Leconte, Lai & Chabrier (2011) developed a model of tidally distorted planets which takes into account the tidally distorted mass distribution within the object assuming an ellipsoidal shape. Burton et al. (2014) studied the consequences of the Roche shape on the measured densities of exoplanets.

The Roche shape of a planet is determined by the semimajor axis, mass ratio, and a value of the surface potential. Assuming the parameters found above ($a = 4.25 \pm 0.11\,{\rm R}_{\odot}$, $M_{\rm A}/M_{\rm b} = 854 \pm 4$ and $R_{\rm b} = 1.554 \pm 0.45\,R_{\rm Jup}$), one can estimate the tidally distorted Roche potential, i.e. the shape of the planet which would have the same cross-section during the transit as the one inferred from the observations under the assumption of a spherical planet. The shape of WASP-103 b is described by the parameters $R_{\rm sub}$, $R_{\rm back}$, $R_{\rm side}$ and $R_{\rm pole}$ (see Budaj 2011 for more details). The descriptions and values of these are given in Table 7. The uncertainties in Table 7 are the quadrature addition of those due to each input parameter; they are dominated by the uncertainty in the radius of the planet.

Table 7. Specification of the shape of WASP-103 b obtained using Roche geometry. $R_{\rm Jup}$, the equatorial radius of Jupiter, is adopted to be 71 492 km.

Symbol	Description	Value
$R_{\rm sub}$ ($R_{\rm Jup}$)	Radius at substellar point	1.721 ± 0.075
$R_{\rm back}$ ($R_{\rm Jup}$)	Radius at antistellar point	1.710 ± 0.072
$R_{\rm side}$ ($R_{\rm Jup}$)	Radius at sides	1.571 ± 0.047
$R_{\rm pole}$ ($R_{\rm Jup}$)	Radius at poles	1.537 ± 0.043
$R_{\rm cross}$ ($R_{\rm Jup}$)	Cross-sectional radius	1.554 ± 0.045
$R_{\rm mean}$ ($R_{\rm Jup}$)	Mean radius	1.603 ± 0.052
$f_{\rm RL}$	Roche lobe filling factor	0.584 ± 0.033
$R_{\rm sub}/R_{\rm side}$		1.095 ± 0.017
$R_{\rm sub}/R_{\rm pole}$		1.120 ± 0.020
$R_{\rm side}/R_{\rm pole}$		1.022 ± 0.003
$R_{\rm back}/R_{\rm sub}$		0.994 ± 0.002
$(R_{\rm mean}/R_{\rm cross})^3$	*Density correction*	1.096 ± 0.015

The cross-sectional radius, $R_{\rm cross} = \sqrt{R_{\rm side} R_{\rm pole}}$, is the radius of the circle with the same cross-section as the Roche surface during the transit. $R_{\rm cross}$ is the quantity measured from transit light curves using spherical-approximation codes such as JKTEBOP. $R_{\rm mean}$ is the radius of a sphere with the same volume as that enclosed by the Roche surface.

Table 7 also gives ratios between $R_{\rm sub}$, $R_{\rm back}$, $R_{\rm side}$ and $R_{\rm pole}$. Moderate changes in the planetary radius lead to very small changes in the ratios. In the case that future analyses yield a revised planetary radius, these ratios can therefore be used to rescale the values of $R_{\rm sub}$, $R_{\rm back}$, $R_{\rm side}$ and $R_{\rm pole}$ appropriately. In particular, the quantity $(R_{\rm mean}/R_{\rm cross})^3$ is the correction which must be applied to the density measured in the spherical approximation to convert it to the density obtained using Roche geometry.

WASP-103 b has a Roche lobe filling factor ($f_{\rm RL}$) of 0.58, where $f_{\rm RL}$ is defined to be the radius of the planet at the substellar point relative to the radius of the L1 point. The planet is therefore well away from Roche lobe overflow but is significantly distorted. The above analysis provides corrections to the properties measured in the spherical approximation. The planetary radius increases by 2.2 per cent to $R_{\rm b} = 1.603 \pm 0.052\,R_{\rm Jup}$, and its density falls by 9.6 per cent to $\rho_{\rm b} = 0.335 \pm 0.025\,\rho_{\rm Jup}$. These revised values include the uncertainty in the correction for asphericity and are included in Table 5. These departures from sphericity mean WASP-103 b is one of the three most distorted planets known, alongside WASP-19 b and WASP-12 b.

6 VARIATION OF RADIUS WITH WAVELENGTH

If a planet has an extended atmosphere, then a variation of opacity with wavelength will cause a variation of the measured planetary radius with wavelength. The light-curve solutions (Table 4) show a dependence between the measured value of k and the central wavelength of the passband used, in that larger k values occur at bluer wavelengths. This implies a larger planetary radius in the blue, which might be due to Rayleigh scattering from a high-altitude atmospheric haze (e.g. Pont et al. 2008; Sing et al. 2011; Pont et al. 2013).

We followed the approach of Southworth et al. (2012) to tease out this signal from our light curves. We modelled each data set with the parameters $r_{\rm A}$ and i fixed at the final values in Table 4, but still fitting for T_0, $r_{\rm b}$, the linear limb darkening coefficient and the polynomial coefficients. We did not consider solutions with both limb darkening

Table 8. Values of r_b for each of the light curves as plotted in Fig. 7. Note that the error bars in this table exclude all common sources of uncertainty in r_b so should only be used to compare different values of $r_b(\lambda)$.

Passband	Central wavelength (nm)	FWHM (nm)	r_b
g	477.0	137.9	0.039 11 ± 0.000 29
r	623.1	138.2	0.038 06 ± 0.000 22
R	658.9	164.7	0.037 70 ± 0.000 10
i	762.5	153.5	0.036 43 ± 0.000 26
I	820.0	140.0	0.037 03 ± 0.000 22
z	913.4	137.0	0.036 98 ± 0.000 33

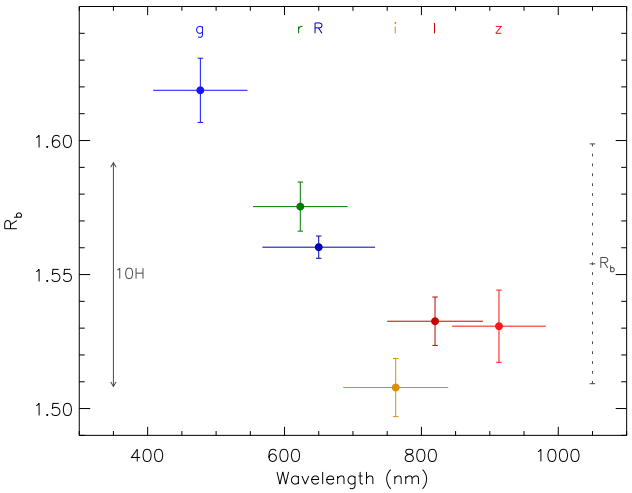

Figure 7. Measured planetary radius (R_b) as a function of the central wavelength of the passbands used for different light curves. The data points show the R_b measured from each light curve. The vertical error bars show the relative uncertainty in R_b (i.e. neglecting the common sources of error) and the horizontal error bars indicate the FWHM of the passband. The data points are colour-coded consistently with Figs 1 and 2 and the passbands are labelled at the top of the figure. The dotted grey line to the right of the figure shows the measured value of R_b from Table 5, which includes all sources of uncertainty. The solid grey line to the left of the figure shows how big 10 pressure scaleheights is.

coefficients fixed, as they had a significantly poorer fit, or with both fitted, as this resulted in unphysical values of the coefficients for most of the light curves. This process yielded a value of r_b for each light curve with all common sources of uncertainty removed from the error bars (Table 8), which we then converted to R_b using the semimajor axis from Table 5. We excluded the CASLEO data from this analysis due to the low precision of the r_b it gave.

Fig. 7 shows the R_b values found from the individual light curves as a function of wavelength. The value of R_b from Table 5 is indicated for context. We calculated the atmospheric pressure scaleheight, H, of WASP-103 b using this formula (e.g. de Pater & Lissauer 2001):

$$H = \frac{k_B T'_{eq}}{\mu g_b}, \quad (1)$$

where k_B is Botzmann's constant and μ is the mean molecular weight in the atmosphere. We adopted $\mu = 2.3$ following de Wit & Seager (2013), and the other parameters were taken from Table 5. This yielded $H = 597$ km $= 0.008\,34\,R_{Jup}$. The relative errors on our individual R_b values are therefore in the region of few pressure scaleheights, and the total variation we find between the *g* and *i* bands is $13.3H$. For comparison, Sing et al. (2011, their fig. 14) found a variation of $6H$ between 330 nm and 1 μm in transmission spectra of HD 189733 b. Similar or larger effects have been noted in transmission photometry of HAT-P-5 (Southworth et al. 2012), GJ 3470 (Nascimbeni et al. 2013) and Qatar-2 (Mancini et al. 2014a).

Is this variation with wavelength plausible? To examine this, we turned to the MassSpec concept proposed by de Wit & Seager (2013). The atmospheric scaleheight depends on surface gravity and thus the planet mass:

$$M_b = \frac{k_B T'_{eq} R_b^2}{\mu G H}, \quad (2)$$

where G is the gravitational constant. The variation of the measured radius with wavelength due to Rayleigh scattering depends on the atmospheric scaleheight under the assumption of a power-law relation between the wavelength and cross-section of the scattering species. Rayleigh scattering corresponds to a power-law coefficient of $\alpha = -4$ (Lecavelier Des Etangs et al. 2008) where

$$\alpha H = \frac{\mathrm{d}R_b(\lambda)}{\mathrm{d}\ln\lambda}, \quad (3)$$

which yields the equation

$$M_b = -\frac{\alpha k_B T'_{eq}[R_b(\lambda)]^2}{\mu G \frac{\mathrm{d}R_b(\lambda)}{\mathrm{d}\ln\lambda}}. \quad (4)$$

We applied MassSpec to our $R_b(\lambda)$ values for WASP-103 b. The slope of R_b versus $\ln\lambda$ is detected to a significance of 7.3σ and corresponds to a planet mass of $0.31 \pm 0.05\,M_{Jup}$. The slope is robustly detected, but gives a planet mass much lower than the mass of $M_b = 1.49 \pm 0.11\,M_{Jup}$ found in Section 5. The gradient of the slope is greater than it should be under the scenario outlined above. We can equalize the two mass measurements by adopting a stronger power law with a coefficient of $\alpha = 19.0 \pm 1.5$, which is extremely large. We conclude that our data are not consistent with Rayleigh scattering so are either affected by additional physical processes or are returning spurious results.

The presence of unocculted starspots on the visible disc of the star could cause a trend in the measured planetary radius similar to what we see for WASP-103. Unocculted spots cause an overestimate of the ratio of the radii (e.g. Czesla et al. 2009; Ballerini et al. 2012; Oshagh et al. 2013), and are cooler than the surrounding photosphere so have a greater effect in the blue. They therefore bias planetary radius measurements to higher values, and do so more strongly at bluer wavelengths. Occulted plage can cause an analogous effect (Oshagh et al. 2014), but we are aware of only circumstantial evidence for plage of the necessary brightness and extent in planet host stars.

The presence of starspots has not been observed on WASP-103 A, which at $T_{eff} = 6110$ K is too hot to suffer major spot activity. G14 found no evidence for spot-induced rotational modulation down to a limiting amplitude of 3 mmag, and our light curves show no features attributable to occultations of a starspot by the planet. This is therefore an unlikely explanation for the strong correlation between R_b and wavelength. Further investigation of this effect requires data with a greater spectral coverage and/or resolution.

7 SUMMARY AND CONCLUSIONS

The recently discovered planetary system WASP-103 is well suited to detailed analysis due to its short orbital period and the brightness

of the host star. These analyses include the investigation of tidal effects, the determination of high-precision physical properties, and the investigation of the atmospheric properties of the planet. We have obtained 17 new transit light curves which we use to further our understanding in all three areas.

The extremely short orbital period of the WASP-103 system makes it a strong candidate for the detection of tidally-induced orbital decay (Birkby et al. 2014). Detecting this effect could yield a measurement of the tidal quality factor for the host star, which is vital for assessing the strength of tidal effects, such as orbital circularization, and for predicting the ultimate fate of hot Jupiters. The prime limitation in attempts to observe this effect is that the strength of the signal, and therefore the length of the observational programme needed to detect it, is unknown. Our high-precision light curves improve the measurement of the time of mid-point of a transit at the reference epoch from 67.4 s (G14) to 4.8 s (this work). There are currently no indications of a change in orbital period, but these effects are expected to take of the order of a decade to become apparent. Our work establishes a high-precision transit timing at the reference epoch against which future observations can be measured.

We modelled our light curves with the JKTEBOP code following the *Homogeneous Studies* methodology in order to measure high-precision photometric parameters of the system. These were combined with published spectroscopic results and with five sets of theoretical stellar models in order to determine the physical properties of the system to high precision and with robust error estimates. We present an error budget which shows that more precise measurements of the $T_{\rm eff}$ and [Fe/H] of the host star would be an effective way of further improving these results. A high-resolution *Lucky Imaging* observation shows no evidence for the presence of faint stars at small (but non-zero) angular separations from WASP-103, which might have contaminated the flux from the system and thus caused us to underestimate the radius of the planet.

The short orbital period of the planet means it is extremely close to its host star: its orbital separation of 0.019 78 au corresponds to only $3.0R_{\rm A}$. This distorts the planet from a spherical shape, and causes an underestimate of its radius when light curves are modelled in the spherical approximation. We determined the planetary shape using Roche geometry (Budaj 2011) and utilized these results to correct its measured radius and mean density for the effects of asphericity.

Our light curves were taken in six passbands spanning much of the optical wavelength region. There is a trend towards finding a larger planetary radius at bluer wavelengths, at a statistical significance of 7.3σ. We used the MassSpec concept (de Wit & Seager 2013) to convert this into a measurement of the planetary mass under the assumption that the slope is caused by Rayleigh scattering. The resulting mass is too small by a factor of 5, implying that Rayleigh scattering is not the main culprit for the observed variation of radius with wavelength.

We recommend that further work on the WASP-103 system includes a detailed spectral analysis for the host star, transit depth measurements in the optical and infrared with a higher spectral resolution than achieved here, and occultation depth measurements to determine the thermal emission of the planet and thus constrain its atmospheric energy budget. Long-term monitoring of its times of transit is also necessary in order to detect the predicted orbital decay due to tidal effects. Finally, the system is a good candidate for observing the Rossiter–McLaughlin effect, due to the substantial rotational velocity of the star ($v \sin i = 10.6 \pm 0.9$ km s^{-1}; G14).

ACKNOWLEDGEMENTS

The operation of the Danish 1.54 m telescope is financed by a grant to UGJ from the Danish Natural Science Research Council (FNU). This paper incorporates observations collected using the Gamma Ray Burst Optical and Near-Infrared Detector (GROND) instrument at the MPG 2.2 m telescope located at ESO La Silla, Chile, program 093.A-9007(A). GROND was built by the high-energy group of MPE in collaboration with the LSW Tautenburg and ESO, and is operated as a PI-instrument at the MPG 2.2 m telescope. We thank Mike Gillon for helpful discussions. The reduced light curves presented in this work will be made available at the CDS (http://vizier.u-strasbg.fr/) and at http://www.astro.keele.ac.uk/~jkt/. J Southworth acknowledges financial support from STFC in the form of an Advanced Fellowship. JB acknowledges funding by the Australian Research Council Discovery Project Grant DP120101792. Funding for the Stellar Astrophysics Centre is provided by The Danish National Research Foundation (grant agreement no. DNRF106). TH is supported by a Sapere Aude Starting Grant from The Danish Council for Independent Research. This publication was supported by grant NPRP X-019-1-006 from Qatar National Research Fund (a member of Qatar Foundation). TCH is supported by the Korea Astronomy & Space Science Institute travel grant #2014-1-400-06. CS received funding from the European Union Seventh Framework Programme (FP7/2007-2013) under grant agreement no. 268421. OW (FNRS research fellow) and J Surdej acknowledge support from the Communauté française de Belgique – Actions de recherche concertées – Académie Wallonie-Europe. The following internet-based resources were used in research for this paper: the ESO Digitized Sky Survey; the NASA Astrophysics Data System; the SIMBAD data base and VizieR catalogue access tool operated at CDS, Strasbourg, France; and the arχiv scientific paper preprint service operated by Cornell University.

REFERENCES

Abe L. et al., 2013, A&A, 553, A49
Ballerini P., Micela G., Lanza A. F., Pagano I., 2012, A&A, 539, A140
Birkby J. L. et al., 2014, MNRAS, 440, 1470
Budaj J., 2011, AJ, 141, 59
Burton J. R., Watson C. A., Fitzsimmons A., Pollacco D., Moulds V., Littlefair S. P., Wheatley P. J., 2014, ApJ, 789, 113
Carter J. A., Yee J. C., Eastman J., Gaudi B. S., Winn J. N., 2008, ApJ, 689, 499
Claret A., 2004, A&A, 424, 919
Czesla S., Huber K. F., Wolter U., Schröter S., Schmitt J. H. M. M., 2009, A&A, 505, 1277
Daemgen S., Hormuth F., Brandner W., Bergfors C., Janson M., Hippler S., Henning T., 2009, A&A, 498, 567
de Pater I., Lissauer J. J., 2001, Planetary Sciences. Cambridge Univ. Press, Cambridge
de Wit J., Seager S., 2013, Science, 342, 1473
Demarque P., Woo J.-H., Kim Y.-C., Yi S. K., 2004, ApJS, 155, 667
Dominik M. et al., 2010, Astron. Nachr., 331, 671
Dotter A., Chaboyer B., Jevremović D., Kostov V., Baron E., Ferguson J. W., 2008, ApJS, 178, 89
Eastman J., Siverd R., Gaudi B. S., 2010, PASP, 122, 935
Enoch B., Collier Cameron A., Parley N. R., Hebb L., 2010, A&A, 516, A33
Gillon M. et al., 2013, A&A, 552, A82
Gillon M. et al., 2014, A&A, 562, L3 (G14)
Goldreich P., 1963, MNRAS, 126, 257
Goldreich P., Soter S., 1966, Icarus, 5, 375
Greiner J. et al., 2008, PASP, 120, 405

Hebb L. et al., 2010, ApJ, 708, 224
Hellier C. et al., 2009, Nature, 460, 1098
Jackson B., Greenberg R., Barnes R., 2008, ApJ, 678, 1396
Jackson B., Barnes R., Greenberg R., 2009, ApJ, 698, 1357
Lecavelier Des Etangs A., Pont F., Vidal-Madjar A., Sing D., 2008, A&A, 481, L83
Leconte J., Lai D., Chabrier G., 2011, A&A, 528, A41
Lendl M., Gillon M., Queloz D., Alonso R., Fumel A., Jehin E., Naef D., 2013, A&A, 552, A2
Levrard B., Winisdoerffer C., Chabrier G., 2009, ApJ, 692, L9
Li S.-L., Miller N., Lin D. N. C., Fortney J. J., 2010, Nature, 463, 1054
Mancini L. et al., 2013, MNRAS, 430, 2932
Mancini L. et al., 2014a, MNRAS, 443, 2391
Mancini L. et al., 2014b, A&A, 562, A126
Mancini L. et al., 2014c, A&A, 568, A127
Maxted P. F. L. et al., 2013, MNRAS, 428, 2645
Nascimbeni V., Piotto G., Pagano I., Scandariato G., Sani E., Fumana M., 2013, A&A, 559, A32
Nikolov N., Chen G., Fortney J., Mancini L., Southworth J., van Boekel R., Henning T., 2013, A&A, 553, A26
Ogilvie G. I., 2014, ARA&A, 52, 171
Ogilvie G. I., Lin D. N. C., 2007, ApJ, 661, 1180
Oshagh M., Santos N. C., Boisse I., Boué G., Montalto M., Dumusque X., Haghighipour N., 2013, A&A, 556, A19
Oshagh M., Santos N. C., Ehrenreich D., Haghighipour N., Figueira P., Santerne A., Montalto M., 2014, A&A, 171, A99
Penev K., Sasselov D., 2011, ApJ, 731, 67
Penev K., Jackson B., Spada F., Thom N., 2012, ApJ, 751, 96
Pietrinferni A., Cassisi S., Salaris M., Castelli F., 2004, ApJ, 612, 168
Pont F., Knutson H., Gilliland R. L., Moutou C., Charbonneau D., 2008, MNRAS, 385, 109
Pont F., Sing D. K., Gibson N. P., Aigrain S., Henry G., Husnoo N., 2013, MNRAS, 432, 2917
Scuflaire R., Théado S., Montalbán J., Miglio A., Bourge P., Godart M., Thoul A., Noels A., 2008, Ap&SS, 316, 83
Seager S., Mallén-Ornelas G., 2003, ApJ, 585, 1038
Sing D. K. et al., 2011, MNRAS, 416, 1443
Skottfelt J. et al., 2013, A&A, 553, A111
Southworth J., 2008, MNRAS, 386, 1644
Southworth J., 2009, MNRAS, 394, 272
Southworth J., 2010, MNRAS, 408, 1689
Southworth J., 2011, MNRAS, 417, 2166
Southworth J., 2012, MNRAS, 426, 1291
Southworth J., Maxted P. F. L., Smalley B., 2004, MNRAS, 349, 547
Southworth J., Wheatley P. J., Sams G., 2007a, MNRAS, 379, L11
Southworth J., Bruntt H., Buzasi D. L., 2007b, A&A, 467, 1215
Southworth J. et al., 2009a, MNRAS, 396, 1023
Southworth J. et al., 2009b, ApJ, 707, 167
Southworth J., Mancini L., Maxted P. F. L., Bruni I., Tregloan-Reed J., Barbieri M., Ruocco N., Wheatley P. J., 2012, MNRAS, 422, 3099
Southworth J. et al., 2014, MNRAS, 444, 776
Stetson P. B., 1987, PASP, 99, 191
Torres G., Winn J. N., Holman M. J., 2008, ApJ, 677, 1324
Tregloan-Reed J., Southworth J., Tappert C., 2013, MNRAS, 428, 3671
VandenBerg D. A., Bergbusch P. A., Dowler P. D., 2006, ApJS, 162, 375

SUPPORTING INFORMATION

Additional Supporting Information may be found in the online version of this article:

Table 2. Sample of the data presented in this work (the first data point of each light curve).
APPENDIX A: Full results for the light curves analysed in this work (http://mnras.oxfordjournals.org/lookup/suppl/doi:10.1093/mnras/stu2394/-/DC1).

Please note: Oxford University Press is not responsible for the content or functionality of any supporting materials supplied by the authors. Any queries (other than missing material) should be directed to the corresponding author for the paper.

[1]*Astrophysics Group, Keele University, Staffordshire ST5 5BG, UK*
[2]*Max Planck Institute for Astronomy, Königstuhl 17, D-69117 Heidelberg, Germany*
[3]*Research School of Astronomy and Astrophysics, Australian National University, Canberra, ACT 2611, Australia*
[4]*Astronomical Institute of the Slovak Academy of Sciences, 059 60 Tatranská Lomnica, Slovakia*
[5]*SUPA, University of St Andrews, School of Physics and Astronomy, North Haugh, St Andrews, Fife KY16 9SS, UK*
[6]*European Southern Observatory, Karl-Schwarzschild-Straße 2, D-85748 Garching bei München, Germany*
[7]*Centre for Star and Planet Formation, Natural History Museum, University of Copenhagen, Øster Voldgade 5-7, DK-1350 Copenhagen K, Denmark*
[8]*Niels Bohr Institute and Centre for Star and Planet Formation, University of Copenhagen, Juliane Maries vej 30, DK-2100 Copenhagen Ø, Denmark*
[9]*Instituto de Astrofisica, Facultad de Fısica, Pontificia Universidad Católica de Chile, Av. Vicuña Mackenna 4860, 7820436 Macul, Santiago, Chile*
[10]*Department of Physics, Sharif University of Technology, PO Box 11155-9161 Tehran, Iran*
[11]*Stellar Astrophysics Centre, Department of Physics and Astronomy, Aarhus University, Ny Munkegade 120, DK-8000 Aarhus C, Denmark*
[12]*Astronomisches Rechen-Institut, Zentrum für Astronomie, Universität Heidelberg, Mönchhofstraße 12-14, D-69120 Heidelberg, Germany*
[13]*Institut d'Astrophysique et de Géophysique, Université de Liège, 4000 Liège, Belgium*
[14]*Qatar Environment and Energy Research Institute, Qatar Foundation, Tornado Tower, Floor 19, PO Box 5825, Doha, Qatar*
[15]*Dipartimento di Fisica 'E.R. Caianiello', Università di Salerno, Via Giovanni Paolo II 132, I-84084 Fisciano (SA), Italy*
[16]*Istituto Nazionale di Fisica Nucleare, Sezione di Napoli, Napoli, I-80126 Napoli, Italy*
[17]*NASA Exoplanet Science Institute, MS 100-22, California Institute of Technology, Pasadena, CA 91125, USA*
[18]*Istituto Internazionale per gli Alti Studi Scientifici (IIASS), I-84019 Vietri Sul Mare (SA), Italy*
[19]*Korea Astronomy and Space Science Institute, Daejeon 305-348, Republic of Korea*
[20]*Finnish Centre for Astronomy with ESO (FINCA), University of Turku, Väisäläntie 20, FI-21500 Piikkiö, Finland*
[21]*Planetary and Space Sciences, Department of Physical Sciences, The Open University, Milton Keynes MK7 6AA, UK*

This paper has been typeset from a TEX/LATEX file prepared by the author.